Revised Manuscript - clean version

Click here to view linked References

This manuscript has been authored in part by UT-Battelle, LLC, under contract DE-AC05-00OR22725 with the US Department of Energy (DOE). The US government retains and the publisher, by accepting the article for publication, acknowledges that the US government retains a nonexclusive, paid-up, irrevocable, worldwide license to publish or reproduce the published form of this manuscript, or allow others to do so, for US government purposes. DOE will provide public access to these results of federally sponsored research in accordance with the DOE Public Access Plan (http://energy.gov/downloads/doe-public-access-plan).

December 2023

Crystal Plasticity Modeling and Analysis for the Transition from Intergranular to Transgranular Failure in Nickel-based Alloy Inconel 740H at Elevated Temperature

Jiahao Cheng[a*], Xiaohua Hu[a], Timothy Lach[b], Xiang (Frank) Chen[b]

[a] Manufacturing Science Division, Oak Ridge National Laboratory, Oak Ridge, TN, USA

[b] Materials Science and Technology Division, Oak Ridge National Laboratory, Oak Ridge, TN, USA

*Corresponding author

Tel.: 865-574-1124

E-mail address: chengj@ornl.gov

Abstract

The precipitation-strengthened Nickel-based alloy Inconel® 740H® (IN740H) exhibits increased ductility at higher applied strain rates during quasi-static tensile tests at an elevated temperature of 760°C. The examination of fracture surfaces in this context reveals a noteworthy transition of underlying fracture mechanisms from transgranular to intergranular fracture as the applied strain rate decreases from $1 \times 10^{-3}/s$ to $0.83 \times 10^{-4}/s$. To thoroughly understand the mechanical response of IN740H under these conditions, this study develops a crystal plasticity finite element (CPFE) model. This model incorporates various deformation mechanisms including dislocation slips, climb, and grain boundary sliding, which are relevant to the test conditions. The model is calibrated using data from both tensile tests at different strain rates and creep tests across a broad stress range at 760°C, enabling the accurate determination of model parameters for each mechanism. Simulation results well captured the experimental observations of different failure modes. At higher strain rates, the model shows a dominance of dislocation slip leading to heterogeneous plastic deformation and formation of transgranular shear bands causing the failure, while at lower strain rates, an increased activity of grain boundary sliding causes grain boundaries crack leading to intergranular failure.

Keywords: negative strain rate sensitivity, intergranular and transgranular fracture, crystal plasticity, Ni-based superalloy

1. Introduction

Inconel® 740H® (IN740H) is a precipitation-strengthened age-hardenable Ni-based superalloy developed by Special Metals Corporation [1]. Compared to the original Inconel 740, IN740H has modified composition, particularly decreased Ti and Si to hinder the formation of G-phase, and increased Al to improve the stability of gamma prime. Moreover, Inconel 740H has a high fraction of low energy coincident site lattices (CSLs) as a result of a good atomic fit. These microstructural features offer a unique combination of high strength and creep resistance at elevated temperatures along with resistance to coal ash corrosion, making IN740H a leading candidate material for emerging harsh environment applications such as advanced ultra-supercritical (A-USC) power plants components. However, unlike most metallic materials whose ductility decreases with increased strain rate, we found IN740H exhibited a negative strain rate sensitivity of failure strain at the service temperature (760^oC) for A-USC. Figures 1a and 1b compare the uniaxial true stress-true strain curves between precipitation-strengthened Ni-based superalloy Haynes® 282® (H282) and IN740H, with more experiment details described in the later section. When subjected to quasi-static strain rates and an elevated test temperature of 760^oC, the H282 samples exhibited very high ductility and underwent necking before fracture, and the failure strain decreased as the applied strain rate increased. In contrast, IN740H showed opposite trend under similar conditions and there was a distinct increasing in the failure strain when the applied strain rate increased. Another factor that more accurately represents the inherent ductility of materials in tensile testing is the reduction of area percentage (RA%) which computes the difference between original cross-sectional area of a specimen and the area of its smallest cross section after failure. As measured and plotted in Figure 1c, it is apparent that for H282, there is a trend of decreasing RA% as the applied strain rate increases, whereas IN740H demonstrates an inverse relationship.

Under quasi-static loading, most ductile metallic materials exhibit a consistent behavior as H282 [2–6]: the effect of raising the strain rate or lowering the temperature is to increase the flow stress and reduce the strain before necking starts, resulting in lower ductility [7]. However, in certain cases the negative strain rate influence on ductility was also observed [7–9]. Kumar et al [10] have conducted tensile testing of IN740H over a large temperature range from room temperature to 800^oC under three different strain rates from $10^{-5}\ s^{-1}$ to $10^{-3}s^{-1}$, and the results showed an

obvious reduction of uniform elongation (the strain to maximum load) with decreased applied strain rate at 600^oC and 800^oC, exhibiting a consistent trend with the data in this work. Marsh [11] has investigated the mechanical properties of Inconel X-750, another γ' precipitation -strengthened nickel-based superalloy under heat treated (aged-hardened) and non-heat treated (solution annealed) conditions, and found both types of samples exhibiting reduced ductility at 650^oC-900^oC as the applied strain rate decreases from $10^{-3}s^{-1}\ to\ 10^{-5}\ s^{-1}$. Asadi et al [12] and Ciesla et al [13] presented the deformation mechanism maps (DMM) for several different γ' precipitation -strengthened nickel-based superalloys and showed near 800^oC is the temperature range where the deformation mechanism transits between dislocation slip, diffusional creep and grain boundary sliding, depending on the applied stress and strain rates. The DMM suggests the negative strain rate sensitivity on ductility or uniform elongation could be associated with the changing of underlying deformation and fracture mechanisms at different strain rates. This can be investigated by examining the fractography of the test samples using scanning electron microscope (SEM), which is plotted in Figures 1d-1f for H282 samples and in Figures 1g-1h for IN740H samples. For H282, the fracture surfaces after testing at $0.83 \times 10^{-4}/s$ to $1 \times 10^{-2}/s$ applied strain rates did not show obvious change of fracture modes, showing typical appearance of 'dimples' from ductile fracture by void formation and coalescence. This observation suggests a consistent deformation and transgranular fracture mechanism in H282 at applied strain rates. For IN740H, the fracture surfaces exhibit clearly different features and transition in the fracture mechanism. At the applied strain rate of $0.83 \times 10^{-4}/s$, the fracture surface shows clear intergranular features with appearance of clear and intact grain boundaries indicating fracture path follows the grain boundaries, whereas at the strain rate of $1 \times 10^{-3}/s$ the fracture surface primarily shows ductile fracture features with occasionally intergranular fracture features as marked in Figure 1h.

The fractography of IN740H reveals a transition in the deformation and fracture mechanism. Based on literature of cast IN740H [14], cavitation damage was observed at the interface between the carbides and the γ grains along grain boundaries following creep and tensile testing at $760^oC - 800^oC$. Based on these observations, we infer the grain boundary creep damage plays a significant role in the failure of IN740H at the low strain rate, causing the intergranular failure.

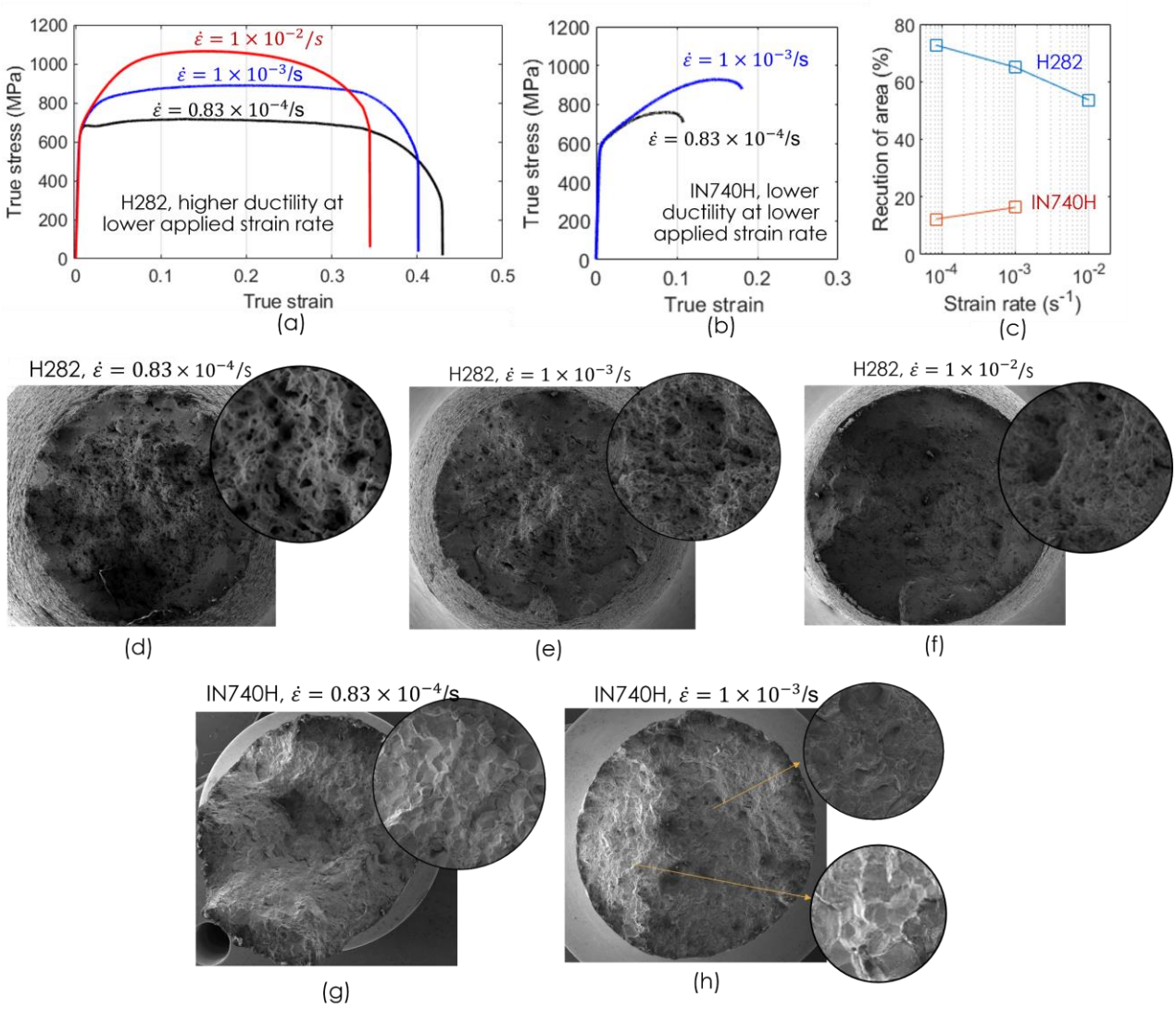

Fig 1. (a,b) stress-strain curves for H282 and IN740, (c) comparison of reduction of area, and (d-h) fractography.

The crystal plasticity finite element (CPFE) method has been widely adopted to model the nickel-based superalloys, considering various hardening mechanisms including the precipitates-strengthening related to dislocation cutting and looping [15,16], anti-phase boundary (APB) resistance [17], back stress related to dislocation pile-up [18], non-Schmid and activation of cubic slip systems [19], creep and rupture mechanisms [20], etc. Using CPFE model to investigate the observed negative strain rate sensitivity of IN740H at the A-USC service-related conditions (760^oC and quasi-static strain rates) has not been well-established yet. Therefore, this work developed a crystal plasticity model considering the grain boundary sliding and damage, as well

as transgranular damage such as through shear banding[21], aiming for modeling the unique tensile and fracture behavior of IN740H, establishing prediction capability and providing more insights.

2. Materials and Experiments

The IN740H used in tensile tests was commercial wrought material in the form of rod with heat HT6308JK produced by Special Metals. The H282 samples, which were used as a reference material for comparison, were from a triple-melt forged disk produced in an advanced ultrasupercritical steam turbines project and more details can be found in [22]. Both materials went through standard age hardening treatment of 1010ºC/2 h and 788ºC/8 h for H282 and 800°C/4 h for IN740H. Smooth cylindrical tensile samples with a gauge diameter of 0.25" and 1.25" gauge length were machined from the raw material. The tensile tests were carried out at a constant temperature of 760^oC under constant engineering strain rate at various strain rates as provided in Figure 1. The samples were characterized for microstructure using electron backscatter diffraction (EBSD) microscope before tensile tests, with the results shown in Figure 2. The EBSD were carried out using a Tescan Mira3 field emission gun SEM equipped with an Oxford Instruments Symmetry high-resolution and high-detection speed EBSD detector.. The samples were sectioned, mounted, grinded, and polished up to a final polishing step with a Buehler VibroMet using 0.05 μm colloidal silica. The EBSD scan was conducted with a beam condition of 30 kV acceleration voltage at a 15 mm working distance, and a 6.63 μm step size for the 740H sample and 1 μm step size for the H282 sample in Figure 2. The EBSD maps h were post-processed and analyzed with MTEX texture analysis package.

IN740H has much coarser grains compared to H282. The average grain size of IN740H is $118\mu m$, while the average grain size of H282 is $25.7\mu m$. Both materials exhibit a weak texture as shown in Figure 2e, indicating the material anisotropy is relatively low. For both materials, a significant amount of annealing twins are observed. The annealing twins do not grow during the tensile tests at 760^oC and therefore no twinning-induced plasticity (TWIP) effect is considered.

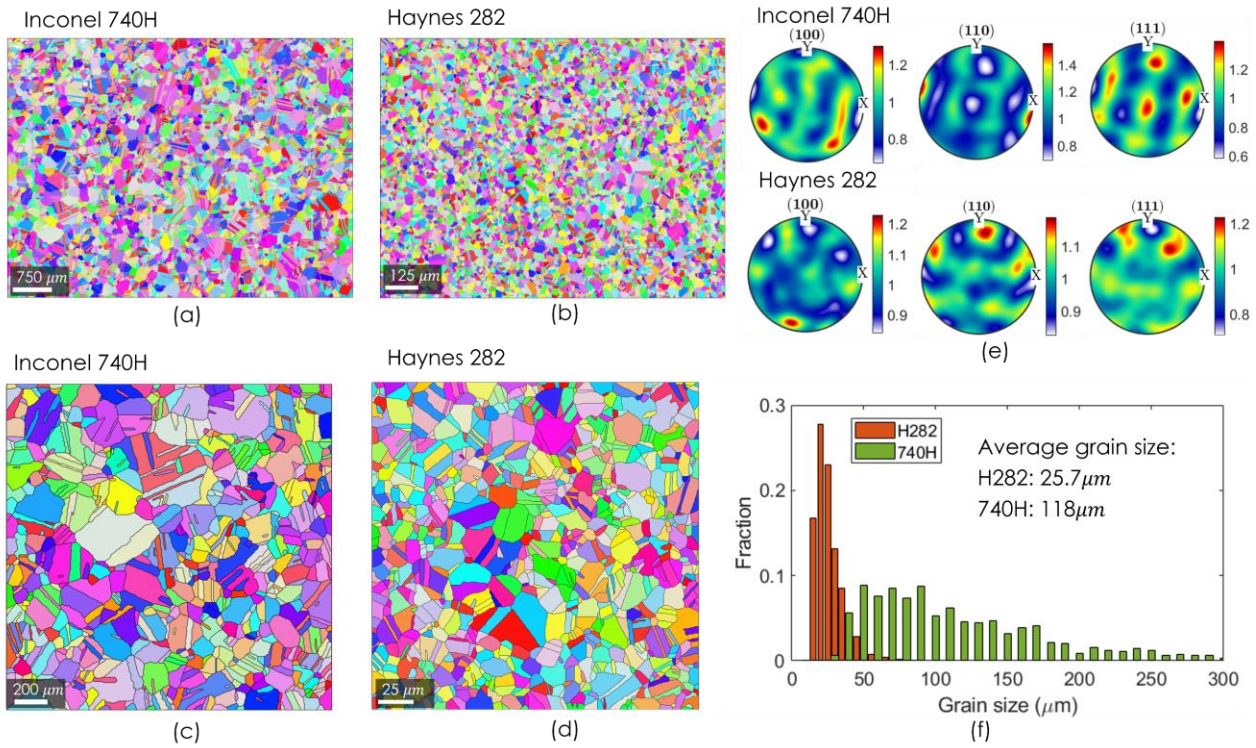

Fig 2. (a,b) Low-magnification and (c,d) High-magnification EBSD images of H282 and IN740H samples before tensile tests. (e) Pole figures showing random texture, and (f) grain size distribution.

3. Model Formulation

The model is based on the hypothesis that at relative higher strain rates, the material deforms dominantly by dislocation glide/slip and material failure occurs by void formation and coalescence in the deformation localized region such as transgranular shear bands. At decreased applied strain rates, the thermally activated diffusion-related mechanism such as dislocation climb and grain boundary sliding becomes more active. When sufficient grain boundary sliding occurs, the grain boundary void or cavities nucleate at local stress concentrators such as near carbides at grain boundaries (Figure 3a), and undergo further growth along grain boundaries through vacancies diffusion at grain boundary or adjacent lattice [23,24]. The continuous void formation at grain boundaries and further loading lead to cracking of grain boundary facets, results in intergranular failure of the material.

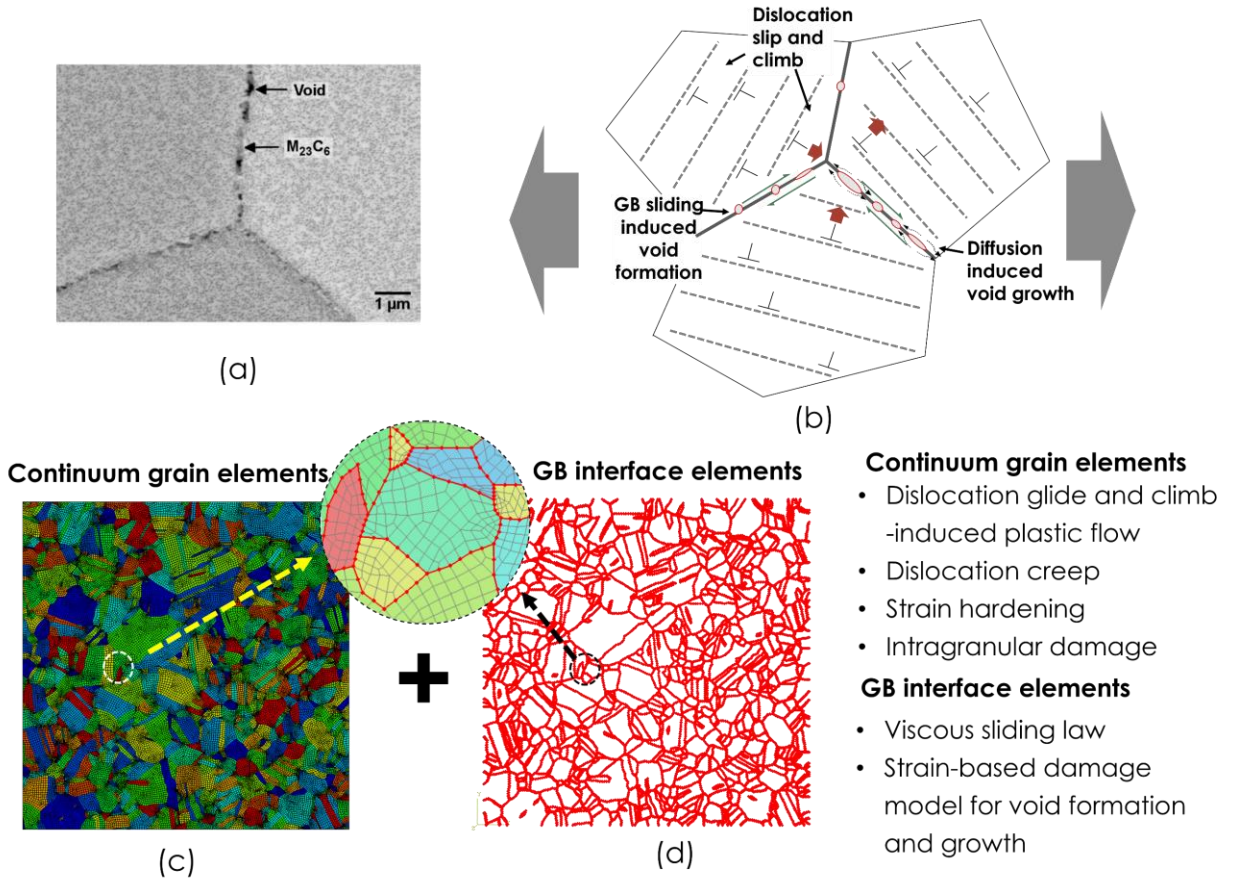

Fig 3. (a) TEM observation of voids and $M_{23}C_6$ carbides in IN740H, figure is from [14]*; (b) schematic showing various deformation mechanisms considered in the CPFE model (c) microstructure meshed with linear continuum elements for grain interior, and (d) cohesive elements inserted at grain boundaries (GB).*

The proposed crystal plasticity model contains two components: (1) the continuum grain lattice region with crystal plasticity constitutive and damage laws, and (2) the grain boundary interfaces modeled with viscous sliding and damage law. In grain interior, continuum elements with linear shape functions are used for meshing (Figure 3c). A rate-dependent, grain-size sensitive crystal plasticity model incorporating the dislocation slip and climb, and evolution of geometrically necessary dislocations (GNDs) [25,26] are used for modeling the plastic flow and hardening at relevant strain rates. The vacancy diffusion-induced dislocation climb model is also critical in this modeling framework because it accommodates grain boundary sliding by relieving the stresses associated with changes in grain boundary shapes and volumes, and plays a key role in describing the strain rate effect on the plastic behavior in the high-temperature and medium-to-low stress

response of Ni-based superalloys [20]. A classic Rice-Tracey damage model [8,27] is also adopted which is known for capturing damage in ductile metals and alloys [25,28]. For grain boundary sliding and damage that leads to intergranular fracture, the cohesive elements are inserted at the interface between grains to represent grain boundaries, and constitutive behavior is captured with a power-law type creep equation and a damage law. The overall model schematic is illustrated in Figure 3. The simulation is conducted using commercial finite element package Abaqus implicit [29] by writing user subroutines, including user-defined material subroutine (UMAT) for the grain elements, and by using user-defined field subroutine (USDFLD) for computing damage of grain boundary cohesive elements.

The key crystal plasticity constitutive equations are summarized as follows:

Kinematic equation:
$$\boldsymbol{F} = \boldsymbol{F}^e \boldsymbol{F}^p \tag{1}$$

Stress − strain relation:
$$\boldsymbol{S} = \mathbb{C}^e : \frac{1}{2}\left(\boldsymbol{F}^e \boldsymbol{F}^{e^T} - \boldsymbol{I}\right) \tag{2}$$

Plastic flow rule:
$$\boldsymbol{L}^p = \dot{\boldsymbol{F}}^p \boldsymbol{F}^{p^{-1}} = \sum_i^{N_{FCC}} \dot{\gamma}_{slip}^i \, \boldsymbol{m}^i \otimes \boldsymbol{n}^i + \sum_j^{N_{FCC}} \dot{\gamma}_{climb}^j \, \boldsymbol{m}^j \otimes \boldsymbol{\chi}^j \tag{3}$$

Slip rate equation:
$$\dot{\gamma}_{\text{slip}}^i = \dot{\gamma}_{slip}^{ref} \left| \frac{\tau_{slip}^i}{g^i} \right|^{\frac{1}{m_s}} sign(\tau^i) \tag{4}$$

Dislocation climb rate:
$$\dot{\gamma}_{climb}^j = \dot{\gamma}_{climb}^{ref} \exp\left(-\frac{F_0}{\kappa\theta}\right) \left| \frac{\tau_{climb}^j}{g_{climb}} \right|^{\frac{1}{m_c}} sign(\tau_{climb}^j) \tag{5}$$

Slip resistance formulation:
$$g^i = \sqrt{\left(g_{SSD}^i\right)^2 + \left(g_{GND}^i\right)^2} \tag{6}$$

SSD Voce hardening law:
$$g^i = g_0^i + \left(g_s^i + \theta_1^i \lambda\right)\left[1 - exp\left(-\left(\frac{\theta_0^i \lambda}{g_s^i}\right)^{\psi}\right)\right] \tag{7}$$

Hall − Petch type initial slip resistance:
$$g_0^i = \hat{g}_0^i + \frac{K^{HP}}{\sqrt{D_g}} \tag{8}$$

Rate − dependent saturation stress:
$$g_s^i = \tilde{g}_s^i + \hat{g}_s^i \log\left(\frac{\dot{\varepsilon}_p}{\dot{\varepsilon}_{ref}}\right) \tag{9}$$

GND hardening law: $$g_{GND} = \tilde{c} G b \sqrt{\rho_{GND}^{tot}} \quad (10)$$

Here, $\boldsymbol{F}$,$\boldsymbol{F}^e$, $\boldsymbol{F}^p$ are the total, elastic and plastic deformation gradients, respectively. **S** is the second Piola-Kirchhoff stress tensor, $\mathbb{C}^e$ is the fourth order elasticity tensor. The plastic flow is represented by plastic velocity gradient tensor $\boldsymbol{L}^p$, which has contributions from dislocation gliding (slip) on slip plane and dislocation climb to overcome non-equilibrium concentrations of point defects. The plastic flow is defined based on the slip at twelve {111}<110> slip systems, where $\dot{\gamma}^i_{\text{slip}}$, $\boldsymbol{m}^i$ and $\boldsymbol{n}^i$ are the slip rate, shear direction vector and slip plane normal vector for i^{th} slip system, respectively. Dislocation climb occurs through vacancies diffusion-assisted movement of dislocation line in perpendicular to its slip plane. The dislocation climb-induced contribution to plastic flow is described by the $\dot{\gamma}^j_{climb}$ the shear strain rate resulted from dislocation climb, the shear direction vector $\boldsymbol{m}^j$ and a unit vector $\boldsymbol{\chi}^j$ which is parallel to the product of normal to the glide plane ($\boldsymbol{n}^j$) and the dislocation line tangent vector ($\boldsymbol{t}^j$). As described in Phan et al [20], the climb tensor can be described in terms of a single parameter ψ which is the angle between dislocation line $\boldsymbol{t}^j$ and $\boldsymbol{m}^j$. This is expressed as :

$$\boldsymbol{m}^j \otimes \boldsymbol{\chi}^j = \left[\boldsymbol{m}^j \otimes \left(\boldsymbol{m}^j \times \boldsymbol{n}^j\right)\right] cos\psi + \left(\boldsymbol{m}^j \otimes \boldsymbol{m}^j\right) sin\psi \quad (11)$$

in this work, $\psi \cong \pi/4$ is assumed in average sense [20], for simplicity. $\{\dot{\gamma}^{ref}_{slip}, m_s, \tau^j_{slip}\}$ and $\{\dot{\gamma}^{ref}_{climb}, m_c, \tau^j_{climb}\}$ are the reference shear rate, strain rate sensitivity parameter and resolved shear stress for slip and climb, respectively. $\dot{\gamma}^{ref}_{slip} = \dot{\gamma}^{ref}_{climb} = 0.001s^{-1}$ is assumed in this work. F_0 is the activation energy for dislocation climb, κ is the Boltzmann constant and θ is the temperature in Kelvin. g_{climb} is a threshold creep stress and treated as a constant in this work. λ is the accumulated slip from all slip systems, i.e. $\lambda = \sum_i^{N_{FCC}} \int_0^t \left|\dot{\gamma}^i\right| dt$. The variable g^i is the total slip resistance, which is composed of g^i_{SSD} and g^i_{GND}, the slip resistance due to statistically stored dislocations (SSDs) and GNDs. The hardening of g^i_{SSD} is modeled by the Voce-type hardening law, where $\theta_0^{micro,i}$, $\theta_1^{micro,i}$ are the initial and linear hardening rate for i^{th} slip system. g^i_0 is the initial slip resistance for i^{th} slip system, which depends on the grain size following Hall-Petch relation. $\hat{g}^i_0$ is the calibratable constant for initial slip resistance, D_g is the grain diameter, and K^{HP} describes the strength of grain boundaries in resisting the slip. $\tilde{g}^i_s$ and $\hat{g}^i_s$ are the constants for rate-dependent slip system saturation stress, and $\dot{\varepsilon}_{ref} = 0.83 \times 10^{-4}/s$ is the reference strain rate.

ρ_{GND}^{tot} is the density of GNDs, G is the effective shear modulus, b is the magnitude of Burger's vector, and $\tilde{c}$=0.01 is a material constant. The computation of GNDs density ρ_{GND}^{tot} evolution depends on the calculation of Nye's dislocation density tensor which is a function of the curl of plastic strain, and the details can be found in [25,30].

The transgranular damage is modeled using a modified Rice-Tracey damage law [14]. This model extends the original Rice-Tracey damage model that describes the void growth by adding Johnson-Cook type strain-rate dependence term and temperature dependence term for the critical strain of failure ε^{crit}, which is expressed as:

$$\varepsilon_{crit}^{p} = d_1 \exp\left(-d_2 \frac{p}{\sigma_{VM}}\right)\left(1 + d_3 \log\left(\frac{\dot{\varepsilon}^{app}}{\dot{\varepsilon}_{ref}}\right)\right)(1 + d_4 T^*) \tag{12}$$

$$\dot{d}^{grains} = \begin{cases} \dfrac{\varepsilon^p - \varepsilon_{crit}^p}{\Delta\varepsilon_d} & if\, \varepsilon^p \geq \varepsilon_{crit}^p \\ 0 & if\ \varepsilon^p < \varepsilon_{crit}^p \end{cases} \tag{13}$$

where $d^{grains} \in [0, d_{max}]$is a damage variable, ε^p is the effective plastic strain, ε_{crit}^p is the critical value for damage initiation, $\Delta\varepsilon_d$ characterize the rate of damage evolution. The upper bound for damage d_{max} is set to 0.99 for better convergence of finite element solver. d_1 is the reference damage initiation value. d_2, d_3 and d_4 are calibratable constants describing the influence from stress triaxiality $\left(\frac{p}{\sigma_{VM}}\right)$, stain rate and temperature (T^*). In this work, the tests are only conducted at a fixed temperature of 760^oC, $d_2 = 0$ and $d_4 = 0$ are assumed for simplicity. Once an element is damaged, its stress is degraded by $\boldsymbol{S} = (1 - d^{macro})\,\widehat{\boldsymbol{S}}$, where the symbol $\widehat{\ }$ indicates the undamaged value.

The grain boundary viscous sliding is modeled using cohesive elements in ABAQUS with a continuum power-law creep model utilizing ABAQUS intrinsic creep module. The constitutive equation is expressed as:

$$\dot{\varepsilon}^v = A\sigma_{vm}^n; \tag{14}$$

In this context, $\dot{\varepsilon}^v$ is the rate of creep strain scaler at grain boundary, and σ_{vm} is the effective von Mises stress at a grain boundary cohesive element. n is a rate-sensitivity parameter for creep and A being a material parameter which essentially represents the inverse of viscosity for n=1. Note

that when employing cohesive elements with continuum constitutive laws in Abaqus, Abaqus assumes that these elements are subjected only to the through-thickness strain components This includes one normal strain component and one shear strain component for two-dimensional case (two shear components for three-dimensional case). The membrane strain components are assumed (enforced by Abaqus) to be zero for the constitutive calculation [29]. The through-thickness and the transverse shear strains are computed based on a constitutive thickness (t_{coh}) which is assumed to be $1\mu m$ here for simplicity. This approach is essentially akin to using traction-separation law for cohesive elements [20,31], with added advantage of allowing using ABAQUS intrinsic creep constitutive laws. The damage at grain boundaries is simply assumed to occur when the creep strain exceeds a threshold value (ε_{crit}^{GB}), and then the cohesive element is removed to effectively simulate grain boundary cracking. The more sophisticated models for grain boundary void nucleation and growth which explicitly account for grain boundary Coble diffusion and adjacent lattice creep, such as in [32,33], are not adopted in this work for ease of computation.

4. Results and Discussion

In this study, the model parameters cannot be solely determined from matching the tensile stress-strain curves, especially the dislocation climb and grain boundary sliding parameters. Since these mechanisms are active in high temperature low-to-medium stress range creep tests, the creep data of IN740H at 750^oC were also used for model calibration. The measured creep data are plotted in Figure4a, along with the literature data from Zhang & Takahashi [34] for the same material received in solution annealed and aged condition following the ASME Code Case 2702 which are consistent with our creep tests samples. A transition of creep strain rate around 300MPa is clearly observed in the literature data, which is also shown but less obvious in our own tests. This transition should correspond to the transition from diffusion-dominated creep to dislocation-dominated creep. The creep simulations are conducted by applying traction boundary conditions in the horizontal surfaces of the CPFE microstructural model and with minimal displacement boundary to constraint rigid body translation and rotations. As shown in Figure 4b, the creep simulations were conducted up to secondary (steady-state) creep stage in order to compute the steady-state creep strain rate. The dislocation slip parameters are calibrated by matching the tensile stress-strain curves prior-to the creep simulation, and then the dislocation climb and grain

boundary sliding parameters are calibrated by matching the creep data, and lastly the parameters are updated in the tensile simulations which are re-conducted to adjust the dislocation slip parameters. This process is repeated until both tensile simulations and creep simulations are both well-matched, as shown in Figure 4a and 5a. The tensile simulations are conducted by applying displacement control in the horizontal surfaces to maintain a constant engineering strain rate condition, which is consistent with experiments. We assume the small temperature difference between creep tests (750^oC) and tensile tests (760^oC) has negligible effect on the model parameters. The damage parameters for grain interior elements and grain boundary cohesive elements are calibrated by matching strain-to-failure in tensile tests at $1 \times 10^{-3}/s$ and $0.83 \times 10^{-4}/s$ strain rates, respectively. It is further noted that the dislocation climb mechanism is critical to calibrate the steady-state creep strain rate as it plays a key role in the dislocation-dominated creep deformation in the high temperature medium stress range (300MPa and 370MPa cases) and it is also important to accommodate the dislocation gliding at the high temperature low stress (<300MPa) range. The final calibrated material parameters are listed in Table 1.

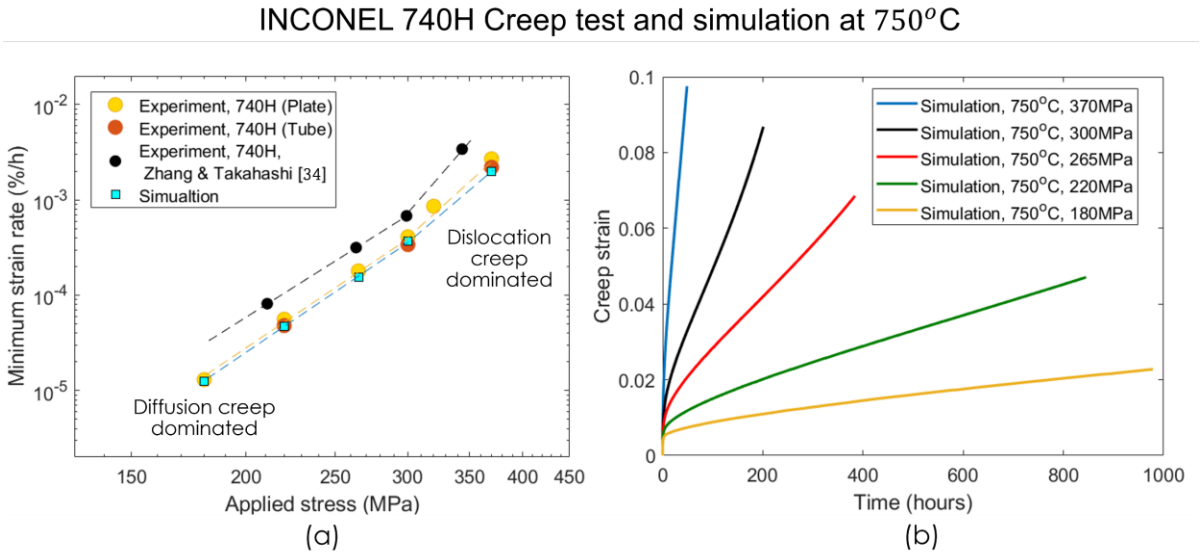

Figure4. (a) Creep experiments and simulation results of steady-state strain rates vs. applied stress plot, and (b) simulation predicted time-creep strain curves.

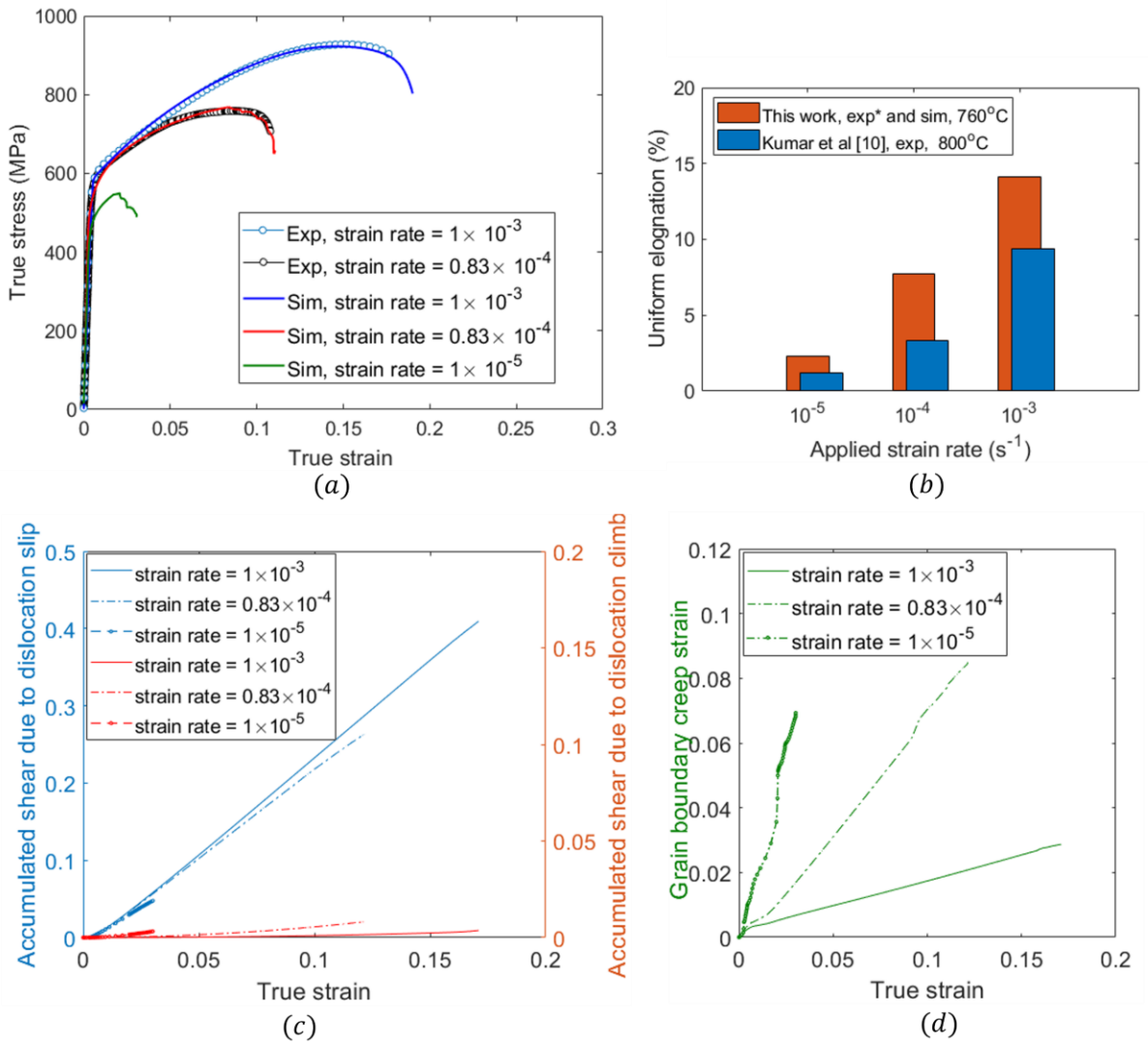

*Figure5. (a) simulation stress-strain curves compared to experiments, (b) comparing the simulation predict reduction of uniform elongation to literature [10]. * Note that in our work, there is no experiment data at applied strain rate of* $1 \times 10^{-5} s^{-1}$ *and only simulation data is available. For the other two applied strain rates, the experiment data and simulation data are well matched. (c-d) The relative activities of various deformation mechanisms. Note that in (d), the grain boundary creep strain is defined as the relative displacement of cohesive nodes over the constitutive cohesive thickness (*$1\mu m$*), and can not be directly compared to the global strain.*

In addition, a simulation at a strain rate of $1 \times 10^{-5} s^{-1}$ was conducted, and the resulting stress-strain curve is also shown in Figure 5a. This further reduction of applied strain rate leads to a very short uniform elongation and hardening period, with stress softening occurring at approximately 2% applied strain. Consequently, the ultimate tensile stress (UTS) is significantly reduced. Although experimental data for this strain rate of $1 \times 10^{-5} s^{-1}$ is unavailable in this study, a recent report by Kumar et al. [25] supports the observed trend. Their tensile tests on IN740H at strain rates ranging from $10^{-5} s^{-1}$ to $10^{-3} s^{-1}$at 800C temperature exhibited the same phenomena that decreasing the applied strain rate correlates with reduced uniform elongation, consistent with our simulation results as shown in Figure 5b. However, due to discrepancies in testing conditions, including temperature (760°C versus 800°C), material preparation, and other variables, their stress-strain data are lower than our simulation results in all applied strain rates. Nevertheless, the observed negative strain rate sensitivity trend suggests that our model accurately captures correct material behavior.

The relative activities of different plastic deformation mechanisms are extracted from tensile simulations and are plotted in Figure 5c and 5d. The low activation energy (F_0) and high strain rate sensitivity (m_c) for dislocation climb make it more active at lower strain rate and less pronounced at higher strain rates, and similarly is the grain boundary sliding. Figure 6 plotted the evolution of strain contour and crack in the CPFE models for $1 \times 10^{-3} s^{-1}$ and $0.83 \times 10^{-4} s^{-1}$strain rate tests, respectively. Noted that the strain in cohesive elements is not visible since they are only at interface (lines for two-dimensional cases). At 9% applied strain, the bulk strain distribution is similar to each other in the two cases as comparing Fig 6a and 6d, but the creep strain at grain boundaries is about two times higher in the $0.83 \times 10^{-4} s^{-1}$ strain rate simulation than that of $1 \times 10^{-3} s^{-1}$ strain rate simulation, as shown in Figure 5d. In the simulation for lower applied strain rates, the sliding-induced creep strain at several grain boundary elements reached the critical strain for grain boundary cracking first before the grain interior had enough plastic deformation for damage to occur, as shown in Figure 6b. The further loading causes these cracks to propagate along grain boundaries and coalescence with other new cracks initiates at other grain boundaries, as shown in Figure 6c, eventually leading to intergranular failure as observed in the experiments (Figure 1g). In contrast, under the applied strain rate of $1 \times 10^{-3}\ s^{-1}$, the grain boundary sliding cannot keep up with the applied strain rate, and the deformation is dominated by dislocation slip in the interior of grains. Therefore, the material continues to deform until damage initiated at 14.5% strain at the

locations with high plastic strain concentration in preferably orientated grains, as shown in Figure 6e. The fully damaged ($d^{grains} = 1$) elements are removed from the microstructure and numerically represents the crack formation. The further loading causes concentrated slip and plastic strain at crack tip as crack propagates, as well as formation of new cracks. The coalescence of cracks in locations of a shear band eventually leads to the transgranular failure, as shown in Fig 6f. These simulation results are consistent with fractography observations, indicating the model captures the correct material deformation and damage trend.

However, we note that the current model is only fitted to the experiment data of IN740H at $760^o\ C$ (the service temperature for A-USC) at $10^{-4} - 10^{-3}s^{-1}$ strain rate range, and informed by literature data at 800^oC and $1 \times 10^{-5}s^{-1}$ strain rate. The model does not consider different temperatures and still needs to be validated for a boarder strain rate range, which will be investigated in future work.

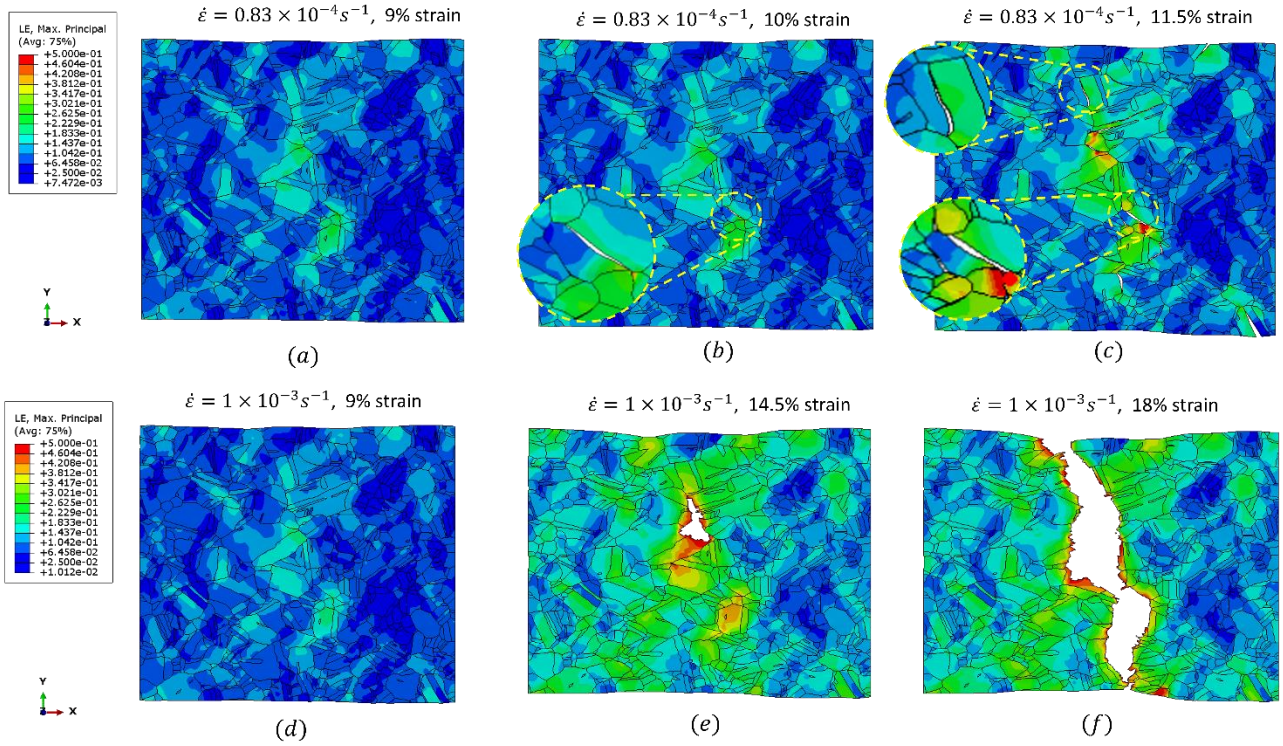

Figure6. Evolution of strain distribution and crack formation in CPFE simulations with (a-c) an applied strain rate of $0.83 \times 10^{-4}s^{-1}$*, and (d-f) an applied strain rate of* $1 \times 10^{-3}s^{-1}$.

Table 1. Calibrated CPFE model parameters

$\hat{g}_0^i$	K^{HP}	g_s^i	g_{climb}	m_s	θ_0^i	θ_1^i	ψ
160 MPa	284MPa*$\mu m^{0.5}$	100MPa	200MPa	0.033	530MPa	20MPa	1.0
m_c	F_0	d_1	d_3	A	n	ε_{crit}^{GB}	
0.16	1.434× 10^{-19}	1.6	0.02	10^{-7}	1.0	0.144	

5. Conclusions

In this work, a crystal plasticity finite element (CPFE) model is developed to capture and analyze the deformation and failure behavior of IN740H Nickel-based alloy at elevated temperature (760^oC) and two different strain rates ($0.83 \times 10^{-4}/s$ and $1 \times 10^{-3}/s$). The IN740H shows a reduced ductility as the applied strain rate is decreased, which is opposite to the same class of precipitation-strengthened alloy such as H282. The negative strain rate sensitivity on ductility is due to the transition of underlying failure mechanism, from the transgranular failure to intergranular failure as the strain rate decreases. The CPFE model considers three deformation mechanisms that are relevant to the material behavior at the corresponding temperature range, including dislocation slips, climb and grain boundary sliding-induced creep deformation. The dislocation slip has a low strain rate sensitivity parameter (m_{slip}) and dominates the plastic deformation at high stress and strain rate regime, while the diffusion-induced dislocation climb and grain boundary sliding are active at high temperature low-to-medium stress range. Both creep tests and tensile tests results at this temperature range are used for fitting the model parameters. The calibrated model showed consistent transition of transgranular to intergranular failure as the strain rates decreased. The intense grain boundary sliding at lower strain rate results in grain boundary cracking before grain interior damage could occur, while at the higher strain rate the material fails by formation of shear bands due to the dominant heterogeneous slip activities in the microstructure. The models and experiments cross-validated our hypothesis about IN740H deformation and failure mechanisms and will be used to further predict and analyze the more complex material response.

Acknowledgement

This project is sponsored by the U.S. Department of Energy (DOE), Office of Fossil Energy and Carbon Management, Crosscutting Research, High Performance Materials Program, under contract DE-AC05-00OR22725 with Oak Ridge National Laboratory (ORNL) managed by UT Battelle, LLC. The Creep data in this study were generated with funding from the DOE Office of Fossil Energy, Crosscutting Technologies program in collaboration with the DOE/ Ohio Economic Development Corporation project on A-USC Materials. We are grateful to V. Cedro III from National Energy Technology Laboratory (NETL) for the programmatic support. We also would like to thank Kelsey Epps from ORNL for performing tensile testing in this project.

Reference

[1] PCC Energy Group, Inconel Alloy 740H: A Superalloy Specifically Designed for Advanced Ultra Supercritical Power Generation, (2014) 1–24. http://www.specialmetals.com/files/PCC EG 740H White Paper.pdf.

[2] J. Xing, L. Hou, H. Du, B. Liu, Y. Wei, A new explanation for the effect of dynamic strain aging on negative strain rate sensitivity in Fe-30Mn-9Al-1C steel, Materials (Basel). 12 (2019). https://doi.org/10.3390/ma12203426.

[3] M. Kawasaki, H.J. Lee, M.C. Oh, B. Ahn, High temperature deformation flow of a ZK60A magnesium alloy after extrusion, Arch. Metall. Mater. 60 (2015). https://doi.org/10.1515/amm-2015-0124.

[4] M.R. Allazadeh, Computing Strain Rate Sensitivity of Aluminium Alloy 1050, Int. Sci. Surv. J. 3 (2020).

[5] L. Bhatta, A. Pesin, A.P. Zhilyaev, P. Tandon, C. Kong, H. Yu, Recent development of superplasticity in aluminum alloys: A review, Metals (Basel). 10 (2020). https://doi.org/10.3390/met10010077.

[6] B. Boldizsár, P. Jenei, A.Q. Ahmed, M.Y. Murashkin, R.Z. Valiev, N.Q. Chinh, Low temperature super ductility and threshold stress of an ultrafine-grained Al–Zn–Mg–Zr alloy processed by equal-channel angular pressing, J. Mater. Sci. 56 (2021). https://doi.org/10.1007/s10853-021-06527-4.

[7] J. Harding, Effect of temperature and strain rate on strength and ductility of four alloy steels, Met. Technol. 4 (1977) 6–16. https://doi.org/10.1179/030716977803292862.

[8] E. El-Magd, Influence of strain rate on ductility of metallic materials, Steel Res. 68 (1997) 67–71. https://doi.org/10.1002/srin.199700544.

[9] E. Cantergiani, G. Falkinger, S. Mitsche, M. Theissing, S. Klitschke, F. Roters, Influence of Strain Rate Sensitivity on Cube Texture Evolution in Aluminium Alloys, Metall. Mater. Trans. A Phys. Metall. Mater. Sci. 53 (2022). https://doi.org/10.1007/s11661-022-06710-5.

[10] C. Kumar, P. Kumar, Analyzing dynamic strain aging and yield strength anomaly in IN740H, a nickel-based superalloy comprising low volume fraction of γ′, Materialia. 33 (2024) 102028. https://doi.org/10.1016/j.mtla.2024.102028.

[11] C. Marsh, The Mechanical Properties and Deformation Behavior of Heat Treated Versus As-Received Inconel X-750, (2018) PhD Thesis.

[12] M. Asadi, D. Guillot, A. Weck, S.R. Hegde, A.K. Koul, T. Sawatzky, H. Saari, Constructing a validated deformation mechanisms map using low temperature creep strain accommodation processes for nickel-base alloy 718, Am. Soc. Mech. Eng. Press. Vessel. Pip. Div. PVP. 2 (2012) 65–73. https://doi.org/10.1115/PVP2012-78092.

[13] M. Cieśla, M. Mańka, F. Binczyk, P. Gradoń, Creep behaviour of modified MAR-247 Superalloy, Arch. Metall. Mater. 61 (2016) 701–704. https://doi.org/10.1515/amm-2016-0119.

[14] J.H. Martin Detrois, Kyle Rozman, Paul Jablonski, Creep Resistant Cast INCONEL Alloy 740H using an Alternative Casting Technique, (2020) TMS. https://www.osti.gov/servlets/purl/1638857.

[15] S. Gupta, C.A. Bronkhorst, Crystal plasticity model for single crystal Ni-based

superalloys: Capturing orientation and temperature dependence of flow stress, Int. J. Plast. 137 (2021) 102896. https://doi.org/10.1016/j.ijplas.2020.102896.

[16] S. Ghorbanpour, M. Zecevic, A. Kumar, M. Jahedi, J. Bicknell, L. Jorgensen, I.J. Beyerlein, M. Knezevic, A crystal plasticity model incorporating the effects of precipitates in superalloys: Application to tensile, compressive, and cyclic deformation of Inconel 718, Int. J. Plast. (2017). https://doi.org/10.1016/j.ijplas.2017.09.006.

[17] S. Ghosh, G. Weber, S. Keshavarz, Multiscale modeling of polycrystalline nickel-based superalloys accounting for subgrain microstructures, Mech. Res. Commun. 78 (2016). https://doi.org/10.1016/j.mechrescom.2015.12.001.

[18] D. Raabe, D. Ma, F. Roters, Effects of initial orientation, sample geometry and friction on anisotropy and crystallographic orientation changes in single crystal microcompression deformation: A crystal plasticity finite element study, Acta Mater. 55 (2007). https://doi.org/10.1016/j.actamat.2007.04.023.

[19] S. Keshavarz, S. Ghosh, A.C.E. Reid, S.A. Langer, A non-Schmid crystal plasticity finite element approach to multi-scale modeling of nickel-based superalloys, Acta Mater. 114 (2016). https://doi.org/10.1016/j.actamat.2016.05.016.

[20] V.T. Phan, X. Zhang, Y. Li, C. Oskay, Microscale modeling of creep deformation and rupture in Nickel-based superalloy IN 617 at high temperature, Mech. Mater. 114 (2017) 215–227. https://doi.org/10.1016/j.mechmat.2017.08.008.

[21] F. Qin, F. Chen, J. Hou, W. Lu, S. Chen, J. Li, Strong resistance to shear instability in multilayered metallic composites by nanoscale amorphous-BCC crystalline interfaces, Mater. Sci. Eng. A. 891 (2024) 145919. https://doi.org/10.1016/j.msea.2023.145919.

[22] R. Purgert, J. Shingledecker, D. Saha, M. Thangirala, G. Booras, J. Powers, C. Riley, H. Hendrix, MATERIALS FOR ADVANCED ULTRASUPERCRITICAL STEAM TURBINES Final Technical Report, (2015).

[23] D.G.C. Syu, A.K. Ghosh, The effect of temperature on the fracture mechanism in 2014A1/15vol.%Al2O3 composite, Mater. Sci. Eng. A. 184 (1994). https://doi.org/10.1016/0921-5093(94)91071-5.

[24] D.M. Parks, Mechanics and mechanisms of creep deformation and damage, Nucl. Eng. Des. 105 (1987). https://doi.org/10.1016/0029-5493(87)90224-X.

[25] J. Cheng, P. Fernandez-Zelaia, Xi. Hu, M. Kirka, Effect of microstructure on fatigue crack propagation in additive manufactured nickel-based superalloy Haynes 282 : an experiment and crystal plasticity study, J. Mater. Sci. (2022). https://doi.org/10.1007/s10853-022-06957-8.

[26] J. Cheng, R. Lane, M. Kesler, J. Brechtl, X. Hu, R. Mirzaeifar, O. Rios, A.M. Momen, K. Nawaza, Experiment and Non-Local Crystal Plasticity Finite Element Study of Nanoindentation on Al-8Ce-10Mg Alloy, Int. J. Solids Struct. 233 (2021) 111233.

[27] J.R. Rice, D.M. Tracey, On the ductile enlargement of voids in triaxial stress fields, J. Mech. Phys. Solids. 17 (1969) 201–217. https://doi.org/10.1016/0022-5096(69)90033-7.

[28] J. Cheng, X. Hu, D. Lancaster, X. Sun, W. Joost, Modeling deformation and failure in AlSi-polyester abradable sealcoating material using microstructure-based finite element simulation, Mater. Des. 219 (2022). https://doi.org/10.1016/j.matdes.2022.110791.

[29] Simulia, Abaqus / CAE 6.14 User's Manual, Dassault Systémes Inc. Provid. RI, USA. (2014) 1–1146.

[30] J. Cheng, S. Ghosh, A crystal plasticity FE model for deformation with twin nucleation in magnesium alloys, Int. J. Plast. 67 (2015) 148–170. https://doi.org/10.1016/j.ijplas.2014.10.005.

[31] M.P. Petkov, E. Elmukashfi, E. Tarleton, A.C.F. Cocks, Evaluation of local stress state due to grain-boundary sliding during creep within a crystal plasticity finite element multi-scale framework, Int. J. Mech. Sci. 211 (2021) 1–28. https://doi.org/10.1016/j.ijmecsci.2021.106715.

[32] X. Jin, R.Z. Wang, Y. Shu, J.W. Fei, J.F. Wen, S.T. Tu, Creep-fatigue crack initiation simulation of a modified 12% cr steel based on grain boundary cavitation and plastic slip accumulation, Materials (Basel). 14 (2021). https://doi.org/10.3390/ma14216565.

[33] O. Nassif, T.J. Truster, R. Ma, K.B. Cochran, D.M. Parks, M.C. Messner, T.L. Sham, Combined crystal plasticity and grain boundary modeling of creep in ferritic-martensitic

steels: I. Theory and implementation, Model. Simul. Mater. Sci. Eng. 27 (2019) 1–42. https://doi.org/10.1088/1361-651X/ab359c.

[34] S. Zhang, Y. Takahashi, Creep and creep-fatigue deformation and life assessment of Ni-based alloy 740H and Alloy 617, Am. Soc. Mech. Eng. Press. Vessel. Pip. Div. PVP. 6A-2018 (2018) 1–11. https://doi.org/10.1115/PVP201885079.

Declaration of interests

☒The authors declare that they have no known competing financial interests or personal relationships that could have appeared to influence the work reported in this paper.

☐The authors declare the following financial interests/personal relationships which may be considered as potential competing interests: